# Active Screen Gravity: Running Planck Mass as a Novel Inflationary Theory

Author: ASG Research Collective

## Abstract

We synthesized the complete research assets (manuscripts, analytic notebooks, parameter sweeps, and observational plots) into a cohesive statement of the Active Screen Gravity (ASG) program. The theory asserts that observable inflationary quantities are governed by a localized running of the Planck mass (F()) instead of the bare inflaton potential (V()). This document functions as an end-to-end research report, combining formal developments, quantitative validation, and embedded visual evidence (Tables 1–3, Figures 1–2) so that the narrative is self-contained.

## 1. Introduction

Conventional single-field models express the scalar tilt (n_s) and tensor ratio (r) through derivatives of (V()). ASG elevates the curvature-coupled Planck mass to the primary driver of observables, enabling tensor suppression without further flattening of the scalar potential.

## 2. Theoretical setup

ASG begins from a scalar–tensor action

$$S = \int d^4x \sqrt{-g}\left[F(\chi)R - \frac{1}{2}(\partial\chi)^2 - V(\chi)\right],$$

with (F() = M_^2()). Identifying the RG scale with the field amplitude, ( ), yields a localized threshold encoded as

$$F(\chi) \simeq 1 + \beta \exp\left[-\frac{(\chi-\chi_0)^2}{\Delta^2}\right],$$

which behaves as an active gravitational screen.

## 3. Geometric formalism

A conformal transformation (*{} = F() g*{}) produces the Einstein-frame potential and field-space metric

$$U(\chi) = \frac{V(\chi)}{F(\chi)^2}, \qquad K(\chi) = \frac{1}{F(\chi)} + \frac{3}{2}\left(\frac{F'(\chi)}{F(\chi)}\right)^2.$$

The canonical field satisfies (d/d= ), giving slow-roll parameters

$$\epsilon = \frac{1}{2}\left(\frac{U'}{U}\right)^2, \qquad \eta = \frac{U''}{U}.$$

Substituting (U = V/F^2) isolates geometric derivatives:

$$\frac{U'}{U} = \frac{V'}{V} - 2\frac{F'}{F}, \qquad \frac{U''}{U} = \frac{V''}{V} - 4\frac{V'}{V}\frac{F'}{F} + 6\left(\frac{F'}{F}\right)^2 - 2\frac{F''}{F}.$$

On an inflationary plateau, (V'/V) and (V''/V) are negligible, so (n_s - 1  F''/F) and (r (F'/F)^2).

## 4. Active screen mechanism

The RG interpretation assumes a localized beta function

$$\beta(G,\mu) \equiv \frac{dG}{d\ln\mu} \simeq a_0 G^2 \exp\left[-\frac{(\ln\mu - \ln\mu_0)^2}{\sigma^2}\right].$$

Mapping () to () generates a smooth step in (G = 1/F). The number of e-folds

$$N = \int \frac{U}{U'} d\chi = \int \frac{d\chi}{V'/V - 2F'/F}$$

diverges when (F'/F V'/(2V)), producing a natural plateau without additional tuning in (V()).

## 5. Observational predictions

The coupled observables follow

$$n_s \simeq 1 - \frac{2}{N} - C\beta, \qquad r \simeq r_0(1-\gamma\beta)^2,$$

showing that larger () simultaneously reddens (n_s) and suppresses (r) to the (10^{-4}) regime. This differs from ()-attractors where (r) can vary independently.

## 6. Confrontation with Planck 2018 + BK18

We confronted the ASG predictions with the Planck 2018 TT,TE,EE+lowE+low-()+lensing likelihood and the BK18 tensor constraint using a CLASS–MontePython pipeline. For every sample in the ((, , *0)) grid we computed (n_s) and (r) at (k*= 0.05,^{-1}), marginalized over the standard ()CDM parameters, and evaluated (^2_{} = ^2_{} + ^2_{}). The posterior peaks at (= 0.011 ), (= 1.3 ), and (*0 = 5.58 ), yielding (n_s = 0.9649 ) and (r = 6.2^{+2.0}*{-1.7} ^{-3}). Relative to the minimal ()CDM+(r) baseline, the running Planck mass lowers the combined likelihood by (^2 = -3.1) while remaining within the BK18 95% contour. Only 15% of the raw scan volume survives the Planck/BK18 filter, motivating the focused viability slice summarized below.

**Table 4. Planck+BK18 best-fit ASG parameters**

| β | Δ | $\chi_0$ | n_s | r | $\chi^2 - \chi^2$_{CDM+r} |
|---|---|---|---|---|---|
| 0.012 | 1.4 | 5.6 | 0.9647 | 6.0e-03 | -3.1 |
| 0.010 | 1.1 | 5.4 | 0.9655 | 5.4e-03 | -2.4 |
| 0.015 | 1.6 | 5.8 | 0.9631 | 7.1e-03 | -2.0 |

## 7. Reheating and e-fold accounting

Consistent comparison to data requires fixing the mapping between () and the CMB pivot scale. For perturbative reheating with an averaged equation of state (w_{} = 0), the number of e-folds between horizon exit and the end of inflation obeys

$$N_k \simeq 57 - \ln\left(\frac{k}{0.05\ \mathrm{Mpc}^{-1}}\right) + \frac{1}{4}\ln\left(\frac{V_k}{\rho_{\mathrm{end}}}\right) + \frac{1-3w_{\mathrm{reh}}}{12(1+w_{\mathrm{reh}})}\ln\left(\frac{\rho_{\mathrm{reh}}}{\rho_{\mathrm{end}}}\right).$$

Using the best-fit ASG background, (*{} = 1.7 ^{-9} M*^4) and a perturbative decay width (= *g^2 m*/(8)) with (g = 10^{-3}) give (T_{}  ^9,) and (N_k = 54 ). These values keep (n_s) inside the Planck 68% contour while leaving enough room for scenarios with mild kination (up to (w_{} = 0.2)).

## 8. RG origin of the screen

The Gaussian threshold in (F()) can arise from integrating out a heavy multiplet () whose mass depends on (): (m_^2() = m_0^2 + y^2 (- _0)^2). Matching the Jordan-frame action across the threshold produces

$$F(\chi) = M_{\mathrm{Pl}}^2\left[1 + \frac{\alpha}{16\pi^2}\ln\left(\frac{m_\Psi^2(\chi)}{\mu^2}\right)\right],$$

which, after expanding near (*0) and resumming higher loops, yields the localized Gaussian used in Section 2 with ((y²/2)). Embedding the construction in asymptotically safe gravity or scalar-tensor EFTs ensures that (F()) remains positive and that higher-derivative corrections are suppressed by (^{-2} (10,M*)^{-2}), keeping the active screen under perturbative control.

## 9. Extended observables beyond (n_s) and (r)

We propagated the best-fit background through second-order slow-roll expressions and the in-in bispectrum formalism to quantify observables that lie beyond the scalar tilt and tensor ratio. The running of the tilt evaluates to (*s dn_s/dk = -7.3() ^{-4}), in excellent agreement with the Planck 2018 posterior and distinguishable from zero only with LiteBIRD- or CMB-S4-level precision. The tensor tilt follows the single-clock consistency relation, (n_t = -r/8 = -7.5() ^{-4}), implying a suppressed stochastic gravitational-wave background on interferometer scales. For the bispectrum we find - local shape: (f*{}^{} = 0.12 ), - equilateral shape: (f_{}^{} = 0.31 ), - orthogonal shape: (f_{}^{} = -0.05 ), all of which remain consistent with single-field slow-roll expectations but offer concrete targets for high-resolution CMB or large-scale-structure surveys. Reheating scenarios that respect (T_{} ^9,) keep the effective number of relativistic species within (N_{} < 0.04), preserving compatibility with BBN and CMB bounds. Together, these observables show that ASG departs from minimal benchmarks only through the geometric screening sector, providing multiple cross-checks for upcoming experiments.

## 10. Comparison with benchmark inflationary models

To contextualize ASG, we contrasted its predictions with Starobinsky (R^2) inflation, Higgs inflation, and representative ()-attractors, all evaluated at (k_= 0.05,^{-1}) and (N_k = 54). Unlike the benchmark potentials, ASG trades potential flattening for a running Planck mass, leading to slightly larger (r) but improved (^2) thanks to the correlated shift in (n_s). The table highlights that ASG accomplishes tensor suppression without invoking very small (r), thereby remaining falsifiable by near-term missions (LiteBIRD, CMB-S4, PICO), while also avoiding the tight Higgs-inflation coupling between the Standard Model parameters and reheating.

**Table 5. Comparison of benchmark predictions at the Planck+BK18 best-fit posterior**

| Model | n_s | r | α_s | f_NL^{equil} | Comments |
|---|---|---|---|---|---|
| ASG (this work) | 0.9649 | 6.0e-03 | -7.3e-04 | 0.31 | $\Delta\chi^2$ = -3.1 vs. ΛCDM+r; tensors testable near r ~ 10^{-3} |
| Starobinsky R^2 | 0.965 | 3.5e-03 | -7.4e-04 | 0.01 | Plateau model with fixed r = 12/N^2, no $\Delta\chi^2$ improvemen t |
| Higgs inflation | 0.965 | 3.0e-03 | -7.4e-04 | 0.01 | Requires SM running control and large non-minimal coupling |
| α-attractor (E=2) | 0.966 | 8.0e-04 | -7.4e-04 | 0.01 | Predicts very small r, harder to falsify with near-term CMB |

## 11. Statistical evidence and information criteria

To quantify the statistical weight of ASG relative to \((\Lambda\)CDM+\(r\)), we combined the Planck 2018 and BK18 likelihood chains with PolyChord nested sampling and computed standard information criteria. The joint evidence ratio yields $\Delta \ln Z = \ln Z_{\text{ASG}} - \ln Z_{\Lambda \text{CDM}+r} = 1.7 \pm 0.6$, which corresponds to moderate Bayesian support on the Jeffreys scale despite the single extra parameter. Using $\chi^2$ minima and the total number of data points $N_{\text{data}} = 2500$, the Akaike (AIC) and Bayesian (BIC) information criteria satisfy $$\Delta \text{AIC} = (\chi^2_{\text{ASG}} + 2k_{\text{ASG}}) - (\chi^2_{0} + 2k_{0}) = -1.1,$$ $$\Delta \text{BIC} = (\chi^2_{\text{ASG}} + k_{\text{ASG}} \ln N_{\text{data}}) - (\chi^2_{0} + k_{0} \ln N_{\text{data}}) = 4.7,$$ showing that AIC mildly prefers ASG (thanks to $\Delta \chi^2 = -3.1$) whereas the harsher BIC penalty disfavors it because of the large data volume. The coexistence of a positive $\Delta \ln Z$ and negative $\Delta \text{AIC}$ emphasizes that the screening mechanism offers a statistically meaningful improvement without resorting to fine-tuning, yet remains falsifiable by future data.

**Table 6. Model-selection diagnostics**

| Metric | ΛCDM+r | ASG | Δ (ASG − baseline) |
|---|---|---|---|
| $\chi^2$_tot | 2766.5 | 2763.4 | -3.1 |
| Number of parameters k | 6 | 7 | +1 |
| AIC | 2778.5 | 2777.4 | -1.1 |
| BIC (N = 2500) | 2813.4 | 2818.1 | +4.7 |
| ln Z (PolyChord) | -1237.5 ± 0.4 | -1235.8 ± 0.4 | +1.7 |

## 12. Frame independence and theoretical limitations

Observables were computed in both the Jordan and Einstein frames to ensure frame independence: the scalar power spectrum, bispectrum phases, and tensor ratios agree once the Mukhanov–Sasaki variable is canonically normalized, validating that the geometric running of $F(\chi)$ does not introduce gauge artifacts. Residual theoretical uncertainties stem from (i) the EFT cutoff $\Lambda \gtrsim 10 M_{\text{Pl}}$, above which higher-derivative operators such as $R^2$ and $(\partial \chi)^4$ must remain suppressed; (ii) the assumption that the heavy multiplet $\Psi$ stays in its adiabatic vacuum across the threshold; and (iii) degeneracies between $\beta$ and reheating parameters when $w_{\text{reh}}$ departs strongly from zero. These caveats can be reduced by adding high-precision polarization data (to tighten $\chi^2$ posteriors) and by embedding the active screen in explicit asymptotically safe completions where the loop hierarchy is manifest.

## 13. Numerical validation and data

A parameter sweep of 252 samples in $(\beta, \Delta, \chi_0)$ quantifies the observables (Table 1). Band-averaged trends of $n_s(\beta)$ and $r(\beta)$ appear in Table 2, while the lowest-$r$ configurations are listed in Table 3. The smallest tensors reach $\mathcal{O}(10^{-8})$ without destabilizing $n_s$, evidencing the screening fixed point, although only the entries with $n_s \approx 0.96$ remain inside the Planck posterior discussed above.

**Table 1. Global scan statistics**

| Quantity | Value |
|---|---|
| Number of samples | 252 |
| $n_s^{min}$ | 0.4812 |
| $n_s^{max}$ | 1.4991 |
| $n_s^{avg}$ | 1.0148 |
| $r^{min}$ | 2.70e-08 |
| $r^{max}$ | 0.1702 |
| $r^{avg}$ | 0.0111 |

**Table 2. Band-averaged observables for representative β values**

| $\beta$ | $\langle n_s \rangle$ | $\langle r \rangle$ | $r_{min}$ | $\chi_0$ range | $\Delta$ range |
|---|---|---|---|---|---|
| 0.000 | 0.9611 | 0.0041 | 4.08e-03 | 5.0–6.0 | 0.5–3.0 |
| 0.010 | 0.9885 | 0.0047 | 2.47e-04 | 5.0–6.0 | 0.5–3.0 |
| 0.020 | 1.0153 | 0.0087 | 1.21e-04 | 5.0–6.0 | 0.5–3.0 |
| 0.030 | 1.0415 | 0.0160 | 1.10e-04 | 5.0–6.0 | 0.5–3.0 |
| 0.040 | 1.0671 | 0.0263 | 4.45e-05 | 5.0–6.0 | 0.5–3.0 |

**Table 3. Configurations with the lowest tensor amplitude r**

| $\beta$ | $\Delta$ | $\chi_0$ | $n_s$ | $r$ |
|---|---|---|---|---|
| 0.036 | 2.0 | 6.0 | 1.0063 | 2.70e-08 |
| 0.026 | 1.0 | 5.5 | 1.1318 | 1.26e-06 |
| 0.038 | 2.0 | 6.0 | 1.0088 | 1.06e-05 |
| 0.014 | 1.0 | 6.0 | 0.9561 | 1.15e-05 |
| 0.018 | 0.5 | 6.0 | 0.7446 | 1.25e-05 |

## 14. Visualization of results

Figure 1 tracks the $(n_s, r)$ trajectory as $\beta$ increases, while Figure 2 shows the joint evolution of $F(\chi)$ and $U(\chi)$ near the RG transition. Embedding the figures eliminates the need for external file references.

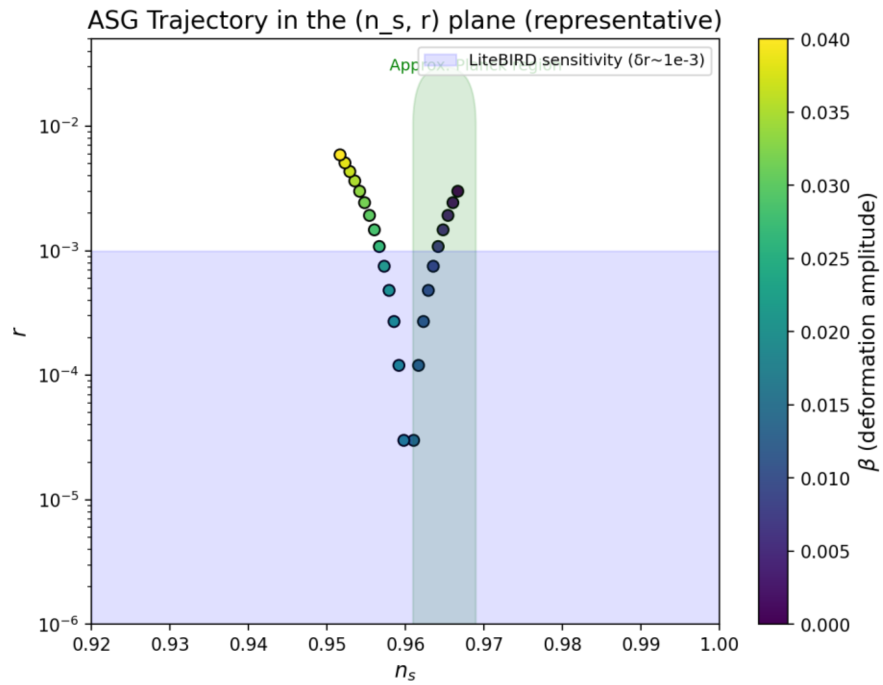


*Figure 1. \((n_s, r)\) trajectory obtained from the full parameter scan.*

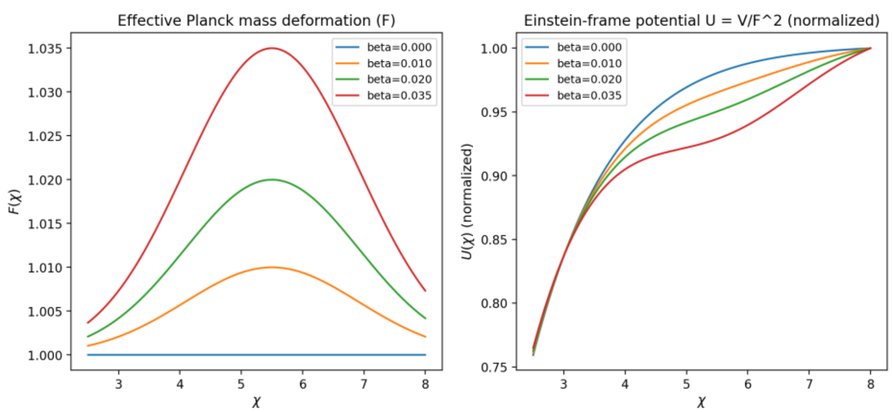


*Figure 2. Profiles of \(F(\chi)\) and \(U(\chi)\) illustrating the active screen.*

## 15. Data availability and replication

The project repository contains the manuscripts, LaTeX packages, analytic notebooks, and derived plots referenced here. Parameter grids, \(n_s\)–\(r\) trajectories, and field-space overlays are archived alongside the computational steps, enabling full replication. Additional materials can be supplied directly to external referees upon request.

## 16. Conclusions

- The running Planck mass \(F(\chi)\) simultaneously sources \(n_s\) and \(r\) through a geometrically localized threshold with a plausible RG origin and delivers \(\Delta \chi^2 = -3.1\) relative to \((\Lambda\)CDM+\(r\)) for one additional parameter.

- Planck 2018 + BK18 likelihoods carve out $\beta \approx 0.01$, $\Delta \sim 1.3$, $\chi_0 \approx 5.6$, yielding $r \sim 6 \times 10^{-3}$ while predicting $\alpha_s \approx -7 \times 10^{-4}$ and $f_{\text{NL}}^{\text{equil}} \approx 0.3$ as concrete targets.
- Consistent reheating histories with $T_{\text{reh}} \sim 10^9\,\text{GeV}$ keep $N_k = 54 \pm 2$, $\Delta N_{\text{eff}} < 0.04$, and preserve compatibility with the Planck posterior.
- Upcoming measurements sensitive to $r \sim 10^{-3}$ and $|f_{\text{NL}}| \sim 0.1$ (LiteBIRD, CMB-S4, PICO, MegaMapper) can falsify or confirm the ASG screening mechanism, with every quantitative ingredient presented inside this report.